Relaxation dynamics in the driven-dissipative Su-Schrieffer-Heeger model

C. M. Dai [1], Yunbo Zhang,[1,*] and X. X. Yi[2,†]

[1]*Key Laboratory of Optical Field Manipulation of Zhejiang Province and Physics Department, Zhejiang Sci-Tech University, Hangzhou 310018, China*

[2]*Center for Quantum Sciences, Northeast Normal University, Changchun 130024, China*

(Received 23 August 2022; accepted 29 November 2022; published 15 December 2022)

For a chain with an open boundary described by the non-Hermitian Hamiltonian, the combination of the algebraic damping and the non-Hermitian skin effect leads to an edge burst. It is interesting to ask whether these features remain when the system is described by a master equation with periodic drives. In this paper, taking the Su-Schrieffer-Heeger model as an example, we explore the relaxation dynamics of the system with time periodically modulated intracell tunneling and single-particle dissipations. We find that for systems with periodic boundary conditions, the relaxation in the infinite-frequency driving limit can be algebraic or exponential depending on the intracell and intercell tunneling amplitudes. Finite-frequency driving can generally open the Liouvillian gap regardless of its strength and can turn the dynamics from algebraic damping to an exponential one. The Liouvillian gap increases with the increase of the driving period until a critical driving period is reached, and then it tends to a small, nonzero value for a sufficiently slow drive. For open boundary systems, we find that the dynamics of the localized excitation is still closely related to the Liouvillian gap before the excitation reaches the system boundary. The propagation speed of the localized excitation that controls the transition relaxation timescale can be slowed down by properly increasing the driving period and amplitude.

DOI: 10.1103/PhysRevA.106.062208

I. INTRODUCTION

Periodic drive is a useful tool to manipulate the properties of closed systems. For example, the topological Bloch band was realized using time-modulated two-dimensional optical lattices [1], the localization feature was changed in the kicked noninteracting one-dimensional quantum system by either time-periodic or nonperiodic pulses [2], and a discrete-time crystal that explicitly reveals the rigidity of the emergent oscillations was predicted in the periodic-driving one-dimensional chain of trapped ions [3]. In recent years, interest in the application of periodic drives (or Floquet engineering) to open quantum systems has grown. Concrete examples include the dynamic control of localization transitions and mobility edges in non-Hermitian quasicrystals [4], dissipative time crystals [5], and driving-assisted open quantum transport [6].

One of the fundamental properties of an open quantum system is the relaxation pattern caused by its couplings to external reservoirs. The control of relaxation time to the steady state plays a crucial role in quantum controls and simulations [7,8]. For open quantum systems described by the Markov master equation, the eigenspectra and eigenmodes of the Liouvillian govern the evolution of the system. The Liouvillian gap defined as the smallest modulus of the real part of nonzero eigenvalues characterizes the asymptotic decay rate to a steady state. It was shown that the localization length of the Liouvillian eigenmodes also plays a crucial role in the transient relaxation of open quantum systems [9].

Recent theoretical works have shown that a tight-binding two-band system described by the Su-Schrieffer-Heeger (SSH) model can have two different types of relaxation behavior in the presence of single-particle dissipation [10]. When the intracell tunneling is larger than the intercell tunneling, the relaxation of this model is algebraic; otherwise, the system shows exponential damping. For the dissipative SSH model with open boundaries, the combination of the algebraic damping and the non-Hermitian skin effect leads to an edge burst [11]. The generalization of the dissipative SSH model by introducing additional spatial modulation of intracell hopping can undergo a chiral to achiral damping transition when the modulation strength increases [12]. It is known that periodic driving can alter the topological phase of matter [1] and change the relaxation behavior of dissipative systems [5]. The dissipative SSH model possesses both rich relaxation behaviors and a non-Hermitian skin effect originating from the intrinsic non-Hermitian topology [13] that leads to boundary-sensitive damping [11]. These motivate us to study how periodic driving enriches the non-Hermitian physics of such a system. Inspired by the method developed in Ref. [10], we will characterize the relaxation process in terms of the damping matrix derived from the Liouvillian of the systems.

The remainder of this paper is organized as follows. In Sec. II we introduce a model and a Floquet theory to describe our periodic-driving system. In Sec. III we investigate the spectral property of the driven-dissipative system. In Sec. IV we study the relaxation dynamics of the system via time

*ybzhang@zstu.edu.cn
†yixx@nenu.edu.cn

evolution of single-particle correlations. Finally, we conclude in Sec. V.

II. MODEL AND FLOQUET THEORY

The starting point of our analysis is the one-dimensional fermionic SSH model [14,15] described by the Hamiltonian

$$H_0 = \sum_x J_0 c_{xA}^\dagger c_{xB} + J_2 c_{xB}^\dagger c_{x+1A} + \text{H.c.}, \tag{1}$$

where $c_{xs}^\dagger$ and c_{xs} are the fermionic creation and annihilation operators, the labels x and $s = A, B$ refer to the unit cell and sublattice, and J_0 and J_2 are the intracell and intercell tunneling amplitudes, respectively. In this work we focus on a driven-dissipative regime where the intracell tunneling amplitude is time periodic modulated and each unit cell is coupled to its environment, leading to the gain or loss of the system. The system Hamiltonian including the drive is

$$H(t) = H_0 + F(t)\sum_x (c_{xA}^\dagger c_{xB} + \text{H.c.}), \tag{2}$$

where $F(t)$ stands for the time-periodic modulation. For simplicity, we choose the piecewise drive,

$$F(t) = \begin{cases} J & 0 \leqslant t < T/2, \\ -J & T/2 \leqslant t < T, \end{cases} \tag{3}$$

where J and T are the driving amplitude and period, respectively. The overall intracell tunneling amplitude is $J_1(t) = J_0 + F(t)$. We set the intracell tunneling strength $J_2 = 1$ as the unit of energy in the following discussions. The evolution of the density matrix $\rho(t)$ of the system is governed by the Lindblad master equation [16],

$$\partial_t \rho(t) = \mathcal{L}(t)[\rho(t)] = -i[H(t), \rho(t)] + \mathcal{D}[\rho(t)], \tag{4}$$

where the dissipator $\mathcal{D}$ describes the quantum jumps caused by coupling to the environment. The dissipator $\mathcal{D}$ is constructed from a set of jump operators $\{L_{x\kappa}\}$,

$$\mathcal{D}(\rho) = \sum_x \sum_{\kappa=\{l,g\}} 2L_{x\kappa}\rho L_{x\kappa}^\dagger - \{L_{x\kappa}^\dagger L_{x\kappa}, \rho\}, \tag{5}$$

where the jump operators are given by

$$\begin{aligned} L_{xl} &= \sqrt{\gamma_l/2}(c_{xA} - ic_{xB}), \\ L_{xg} &= \sqrt{\gamma_g/2}(c_{xA}^\dagger + ic_{xB}^\dagger), \end{aligned} \tag{6}$$

which describe single-particle loss L_{xl} and gain L_{xg} in the unit cell x. The jump operators in Eq. (6) can be realized by coupling both sites in the unit cell to a shared reservoir that induces nonlocal electron loss or gain [17]. A similar model without drive was studied in Ref. [10].

The formal solution of the master equation (4) can be written as $\rho(t) = \mathcal{V}(t, 0)[\rho(0)]$, where $\mathcal{V}(t, 0)$ represents the propagator from the initial time to a given time t. Because the Liouvillian $\mathcal{L}(t)$ of our model is time periodic, i.e., $\mathcal{L}(t) = \mathcal{L}(t + T)$, the propagator over integer multiples of the driving period nT can be factorized as $\mathcal{V}(nT, 0) = \mathcal{V}^n(T, 0)$. We can define a time-independent Floquet generator $\mathcal{L}_F$ [18,19] that reproduces the evolution over one driving period, i.e.,

$$\mathcal{V}(T, 0) = \exp(\mathcal{L}_F T), \tag{7}$$

and rewrite the stroboscopic propagator as $\mathcal{V}(nT, 0) = \exp(\mathcal{L}_F nT)$. In fact, according to the divisibility of the propagator $\mathcal{V}(t, 0)$ [18,20], we can rewrite it as

$$\mathcal{V}(t, 0) = \mathcal{K}(t)\exp(\mathcal{L}_F t), \tag{8}$$

where $\mathcal{K}(t) = \mathcal{K}(t + T)$ is a time-periodic linear operator [18]. In the long-time limit, the density matrix $\rho(t)$ will relax towards a time-periodic steady state [18,21],

$$\rho_s(t) = \mathcal{K}(t)(\rho_F), \tag{9}$$

where we define $\rho_F = \lim_{t\to\infty} \exp(\mathcal{L}_F t)[\rho(0)]$ [18,21].

We are interested in the relaxation process of the system to the time-periodic steady state $\rho_s(t)$. In particular, we focus on the time evolution of the single-particle correlation matrix $\phi(t)$; its elements are given by

$$\phi_{mn}(t) = \text{Tr}[c_m^\dagger c_n \rho(t)], \tag{10}$$

where the index m (or n) labels both the unit cell and sublattice degrees of freedom. We can obtain the evolution equation of the single-particle correlation matrix using the Lindblad master equation (4) (see the Appendix for the details of the derivation),

$$\partial_t \phi(t) = i[h^T(t), \phi(t)] - \left\{M_l^T + M_g, \phi(t)\right\} + 2M_g, \tag{11}$$

where all three matrices $h(t)$, M_l, and M_g are Hermitian matrices. The matrix elements of $h(t)$ are $h_{xA,xB}(t) = h_{xB,xA}^*(t) = J_1(t)$, $h_{xB,x+1A} = h_{x+1A,xB}^* = J_2$, and zero otherwise. The elements of M_l and M_g are $(M_l)_{mn} = \sum_x D_{xl,m}^* D_{xl,n}$ and $(M_g)_{mn} = \sum_x D_{xg,m}^* D_{xg,n}$, where the nonzero elements of matrix D are $D_{xl,xA} = iD_{xl,xB} = \sqrt{\gamma_l/2}$ and $D_{xg,xA} = -iD_{xg,xB} = \sqrt{\gamma_g/2}$. By introducing a non-Hermitian damping matrix

$$X(t) = ih^T(t) - M_l^T - M_g, \tag{12}$$

Eq. (11) can be rewritten into a more compact form,

$$\partial_t \phi(t) = X(t)\phi(t) + \phi(t)X^\dagger(t) + 2M_g. \tag{13}$$

When the system evolves into the steady state $\rho_s(t)$, the single-particle correlation matrix $\phi(t)$ is given by a time-periodic matrix $\phi_s(t) = \phi_s(t + T)$ with elements $[\phi_s(t)]_{mn} = \text{Tr}[c_m^\dagger c_n \rho_s(t)]$. Note that $\phi_s(t)$ satisfies Eq. (13), and one can verify that $\phi_s(t) = \gamma_g \mathbf{1}/\gamma$ using the relation $M_l^T + M_g = M_g\gamma/\gamma_g$, where $\mathbf{1}$ represents the identity matrix and $\gamma = \gamma_l + \gamma_g$.

The convergence of the correlation matrix $\phi(t)$ to its steady-state value $\phi_s(t)$ can be tracked from the deviation

$$\eta(t) = \phi(t) - \phi_s(t). \tag{14}$$

Because both $\phi(t)$ and $\phi_s(t)$ are solutions of Eq. (13), the evolution of the deviation $\eta(t)$ satisfies the following equation:

$$\partial_t \eta(t) = X(t)\eta(t) + \eta(t)X^\dagger(t), \tag{15}$$

and its formal solution is

$$\eta(t) = V(t)\eta(0)V^\dagger(t), \tag{16}$$

where the propagator $V(t)$ can be obtained by solving the equation $\partial_t V(t) = X(t)V(t)$ with the initial condition $V(0) = \mathbf{1}$. Because the damping matrix $X(t)$ inherits the time

periodicity of the Liouvillian $\mathcal{L}(t)$, we can use Floquet theory [20] to factorize $V(t)$ as

$$V(t) = P(t)\exp(X_F t), \tag{17}$$

where the matrix $P(t) = P(t+T)$ describes the micromotion over one driving period and the time-independent matrix X_F controls the long-time evolution of the system. We call X_F the Floquet damping matrix in the following. By setting $t = 0$ in Eq. (17), we have $P(0) = \mathbf{1}$, and what follows is

$$V(T) = \exp(X_F T) = \exp[X(T/2)T/2]\exp[X(0)T/2]. \tag{18}$$

Generally, X_F is also a non-Hermitian matrix, and we can expand it by the left ($|u_n^L\rangle$) and right ($|u_n^R\rangle$) eigenvectors [22,23],

$$X_F = \sum_n \lambda_n |u_n^R\rangle\langle u_n^L|, \tag{19}$$

where the eigenvectors satisfy the eigenvalue equations $X_F|u_n^R\rangle = \lambda_n|u_n^R\rangle$ and $X_F^\dagger|u_n^L\rangle = \lambda_n^*|u_n^L\rangle$, respectively. We have biorthonormality between the two complete sets of eigenvectors $\{|u_n^R\rangle\}$ and $\{|u_n^L\rangle\}$, $\langle u_{n'}^L|u_n^R\rangle = \delta_{nn'}$ [22]. Using the expansion (19) and the factorization (17), we can write the formal solution (16) as

$$\eta(t) = \sum_{n,n'} \exp[(\lambda_n + \lambda_{n'}^*)t]|u_n^R(t)\rangle\langle u_n^L|\eta(0)|u_{n'}^L\rangle\langle u_{n'}^R(t)|, \tag{20}$$

where $|u_n^R(t)\rangle = P(t)|u_n^R\rangle$ is time periodic. It is illuminating to consider the spectrum of X_F for a closed system, i.e., $\gamma_l = \gamma_g = 0$. The eigenvalue λ_n is purely imaginary, and $|u_n^R\rangle = |u_n^L\rangle$. The coupling to the environment brings the system to a steady state after a period of evolution. The real part of λ_n captures the lifetimes of the different eigenmodes, and we have $\mathrm{Re}(\lambda_n) \leqslant 0$. One crucial quantity that determines the long-time relaxation dynamics is the Liouvillian gap [10,24], defined as $\Lambda = \min[2\mathrm{Re}(-\lambda_n)]$. It is known that a finite gap leads to exponential convergence to the steady state, and for the case of a vanishing gap, the convergence to the steady state is algebraic [10].

III. FLOQUET SPECTRUM

Before exploring the relaxation dynamics of our model, we first study the eigenvalue spectrum of the Floquet damping matrix X_F, which contains useful information about the dynamic properties of the system. In the case of periodic boundary conditions, it is convenient to transform the damping matrix $X(t)$ to the momentum space by the relation $|xs\rangle = \sum_k \exp(-ikx)|ks\rangle/\sqrt{N}$, where N is the number of unit cells. In the momentum space, the damping matrix reads

$$X(k,t) = i[(J_1(t) + J_2\cos k)\sigma_x + (J_2\sin k - i\gamma/2)\sigma_y] - \gamma/2, \tag{21}$$

and the corresponding k-dependent Floquet damping matrices $X_F(k)$ are given by

$$\exp[X_F(k)T] = \exp[X(k,T/2)T/2]\exp[X(k,0)T/2]. \tag{22}$$

For the case of weak ($J \ll 1$) and high-frequency drive ($1/T \gg 1$), we can calculate the approximate Floquet damping matrix $X_F(k)$ using the Baker-Campbell-Hausdorff (BCH) formula [25],

$$\exp A \exp B = \exp\{A + B + [A,B]/2 + [[A,B],B]/12 + [A,[A,B]]/12 + \cdots\}, \tag{23}$$

and then find its eigenvalues. For general driving parameters that are not subject to these limits, we solve the eigenvalue equation numerically to obtain the Floquet spectrum.

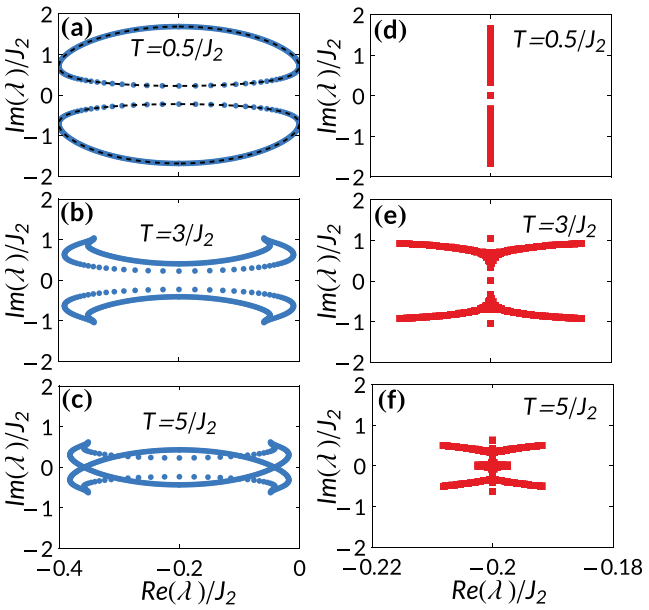

FIG. 1. Eigenvalue spectrum of the effective damping matrix X_F for a few increasing driving periods T. (a)–(c) are the results of the periodic boundary chain, and (d)–(f) show the cases with the open boundary chain. The black dashed lines in (a) indicate the results obtained by the zeroth-order effective damping matrix $X_F^{(0)}(k)$. The parameters used in the calculations are $J_0 = 0.7J_2$, $J = 0.2J_2$, and $\gamma_g = \gamma_l = 0.2J_2$, and the number of unit cells $N = 200$.

According to the BCH formula, the approximate damping matrix up to zeroth order in terms of driving period T is

$$X_F^{(0)}(k) = [X(k,0) + X(k,T/2)]/2 = i[(J_0 + J_2\cos k)\sigma_x + (J_2\sin k - i\gamma/2)\sigma_y] - \gamma/2. \tag{24}$$

This is exactly the same damping matrix that was studied in Ref. [10]. If $J_0 \leqslant J_2$, the Liouvillian gap of $X_F^{(0)}(k)$ closes at

$$k_\pm^0 = \pi \pm \arccos(J_0/J_2), \tag{25}$$

and there is a nonzero Liouvillian gap when $J_0 > J_2$ [10]. Therefore, in the fast-driving limit $T \to 0$, with a suitable choice of the tunneling amplitudes J_0 and J_2, the Liouvillian gap can still be closed.

In Fig. 1(a), we plot the spectra of $X_F^{(0)}(k)$ (dashed line) and $X_F(k)$ (blue dotted line) for fast driving $T = 0.5/J_2$; we can see that the overall shapes of their spectra are similar to each other. However, the difference between $X_F^{(0)}(k)$ and $X_F(k)$ arises when we consider the size of their Liouvillian gaps. For example, when we take the system parameters in Fig. 1(a), $X_F^{(0)}(k)$ is gapless, but $X_F(k)$ has a nonvanishing Liouvillian

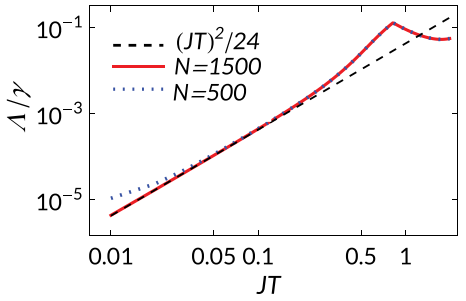

FIG. 2. Normalized Liouvillian gap as a function of the dimensionless parameter JT. The solid and dotted lines denote the results for systems with unit cells $N = 1500$ and 500, respectively. The dashed line represents the approximate analytic result $(JT)^2/24$. The other parameters used are $J_0 = 0.7J_2$, $J = 0.2J_2$, and $\gamma_g = \gamma_l = 0.2J_2$.

gap $\Lambda \approx 2 \times 10^{-4} J_2$, although the gap is too small to see in Fig. 1(a). Larger Liouvillian gaps can be obtained when the drives with longer periods are used, as shown in Figs. 1(b) and 1(c) for two relatively slow drivings with $T = 3/J_2$ and $T = 5/J_2$, respectively.

In order to capture the dependence of the Liouvillian gaps on the driving parameters, we expand the effective damping matrix up to the second power of driving period by the BCH formula; the result is

$$X_F^{(2)}(k) = X_F^{(0)}(k) + JT(\gamma + 2iJ_2 \sin k)(3\sigma_z - JT\sigma_y)/12, \tag{26}$$

where the second term on the right side of the equation with the complex coefficient $\gamma + 2iJ_2 \sin k$ suggests that the corrections to the zeroth-order damping matrix $X_F^{(0)}(k)$ contain both incoherent and coherent parts, although only the coherent intracell tunneling amplitude $J_1(t)$ is modulated periodically. Note that according to the complex Hurwitz test [26], if we expand $X_F(k)$ up to linear order in the driving period T, i.e., $X_F^{(1)}(k) = X_F^{(0)}(k) + JT(\gamma + 2iJ_2 \sin k)\sigma_z/4$, the eigenvalues of $X_F^{(1)}(k)$ can have a nonphysical positive real part when $k = k_\pm^0$ in the case of $J_1 < J_2$ and any nonzero T. This problem does not arise in the second-order expansion $X_F^{(2)}(k)$ for a sufficiently short driving period. We find that the values of k that make the eigenvalues of $X_F^{(2)}(k)$ have the largest real part are still $k_\pm^0$; then the approximate Liouvillian gap given by $X_F^{(2)}(k)$ is

$$\Lambda^{(2)} = \gamma(1 - \sqrt{36 - 3J^2T^2 + J^4T^4}/6) \approx \gamma(JT)^2/24, \tag{27}$$

which satisfies the power-law scaling relation as a function of the product JT. This equation also suggests that the specific choice of J_0 and J_2 (assuming $J_0 < J_2$) does not affect the size of the Liouvillian gap for fast driving.

In Fig. 2, we compare the analytical result $\Lambda^{(2)} \approx \gamma(JT)^2/24$ with the numerical solution of the Liouvillian gap. The analytical result in Fig. 2 is indicated by the dashed line, and the numerical results are denoted by the dotted and solid lines for systems with two different lengths, $N = 500$ and $N = 1500$, respectively. We can see that the results for $N = 500$ are slightly larger than the case with $N = 1500$ when $JT \approx 0.01$. This difference originates from the fact that k can take discrete values only when the size of the system is finite; for larger N, the interval between the two adjacent k gets closer, and the Liouvillian gap tends to the continuum-limit result. When the driving is fast, i.e., $JT \lesssim 0.2$, the analytic result shows good agreement with the numerical solutions. The departure between the analytic and numerical results in Fig. 2 for $JT \gtrsim 0.2$ suggests that the validity of the damping matrix $X_F^{(2)}$ gradually breaks down with the increasing of the driving period T.

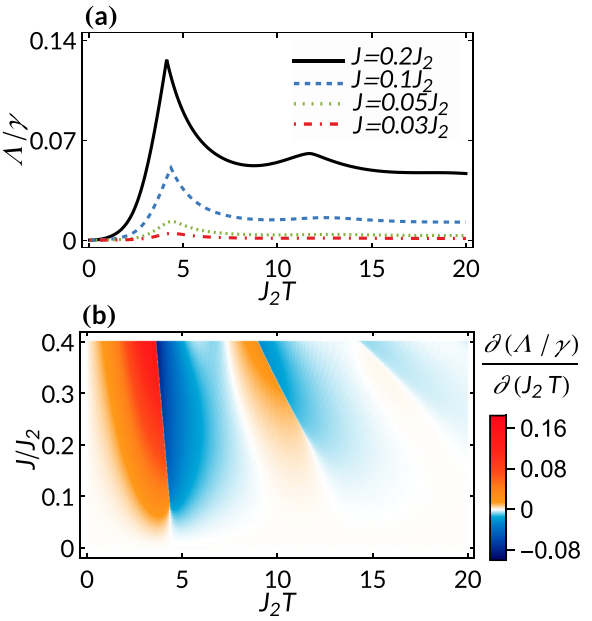

FIG. 3. (a) Liouvillian gap Λ as a function of driving period T. The results for the four different driving amplitudes $J = 0.2J_2$, $0.1J_2$, $0.05J_2$, and $0.03J_2$ are denoted by different types of lines. (b) The first derivative of the Liouvillian gap versus driving period T as a function of the driving period T and amplitude J. The other parameters are $J_0 = 0.7J_2$, $J = 0.2J_2$, and $\gamma_g = \gamma_l = 0.2J_2$.

We show the Liouvillian gap Λ for a few different driving amplitudes J and a wide range of driving periods T in Fig. 3(a). The results demonstrate that regardless of the specific driving amplitude used, the Liouvillian gap increases along with the increasing of the driving period until the maximum is reached; then it starts to decrease and tends to a nonzero value for large enough T. When the driving is strong enough, for example, $J = 0.2J_2$, as shown in Fig. 3(a) by the black solid line, multiple local maxima can appear. We can see that there are two different typical behaviors of the Liouvillian gap as a function of the driving period near its maximum. For the relatively weak drives $J = 0.03J_2$ and $0.05J_2$, there is a smooth crossover of the Liouvillian gap from increasing to decreasing. But for the case of strong driving with $J = 0.1J_2$ and $0.2J_2$, the transition is not smooth.

To clarify this point, we plot the first partial derivative of the Liouvillian gap versus the driving period $\partial\Lambda/\partial T$ as a function of J and T in Fig. 3(b). We can see that for larger J, $\partial\Lambda/\partial T$ changes abruptly from positive to negative values when T increases to nearly $4/J_2$, and there is a smooth crossover only when J is small. If the driving is strong enough, $\partial\Lambda/\partial T$ as a function of T can have multiple discontinuity

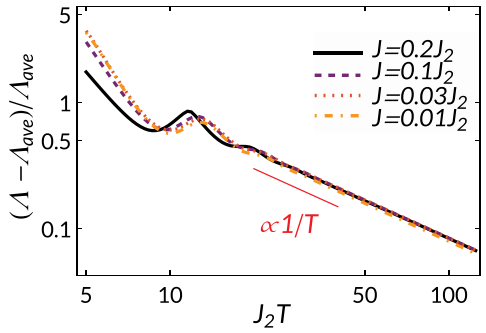

FIG. 4. The relative deviation between Λ and $\Lambda_{\rm ave}$ as a function of the driving period T. The results for four different driving amplitudes J are denoted by different lines. The other parameters are $J_0 = 0.7J_2$ and $\gamma_g = \gamma_l = 0.2J_2$. The thin red line represents the power-law fitting.

points where Λ obtains extreme values. For example, when $J = 0.4J_2$, the second discontinuity point is located at $T \approx 9/J_2$, as shown in Fig. 3(b). Note that these specific driving periods which make Λ take extreme values rely on the system parameters and show roughly linear dependence on the driving amplitude J [see Fig. 3(b)].

As for the behavior of the Liouvillian gap when T is large, we find that it satisfies a quite compact expression in the slow-driving limit $T \to \infty$,

$$\lim_{T\to\infty} \Lambda = \Lambda_{\rm ave} = \min\{-{\rm Re}[\tilde{\lambda}_1(k, T/2) + \tilde{\lambda}_1(k, 0)]\}, \quad (28)$$

where $\tilde{\lambda}_1(k,t)$ denotes the eigenvalue of $X(k,t)$ with the largest real part for given k and t. This means that the Liouvillian gap can be inferred from the time average of the k-dependent instantaneous damping rate when the driving is slow enough. A comparison of Λ and $\Lambda_{\rm ave}$ for finite T is shown in Fig. 4, where the relative deviation between Λ and $\Lambda_{\rm ave}$ decreases as a power law of the driving period T. In order to obtain Eq. (28), we start with the right eigenvector $|\tilde{\lambda}_1^R(k, T/2)\rangle$ corresponding to the eigenvalue $\tilde{\lambda}_1(k, T/2)$. It is easy to find that

$$\begin{aligned}&\exp[X(k,0)T/2]\big|\tilde{\lambda}_1^R(k,T/2)\big\rangle\\ &\quad\approx \zeta_1 \exp[\tilde{\lambda}_1(k,0)T/2]\big|\tilde{\lambda}_1^R(k,0)\big\rangle\end{aligned} \quad (29)$$

for large T, where we define

$$\zeta_1 = \big\langle\tilde{\lambda}_1^L(k,0)\big|\tilde{\lambda}_1^R(k,T/2)\big\rangle$$

and $|\tilde{\lambda}_1^{R(L)}(k,0)\rangle$ stands for the right (left) eigenvector corresponding to the eigenvalue $\tilde{\lambda}_1(k,0)$. Equation (29) holds because the mode described by $|\tilde{\lambda}_1^R(k,0)\rangle$ decays the most slowly for the given k. For the same reason, we have

$$\begin{aligned}&\exp[X(k,T/2)T/2]\exp[X(k,0)T/2]\big|\tilde{\lambda}_1^R(k,T/2)\big\rangle\\ &\approx \zeta\exp\{[\tilde{\lambda}_1(k,0)+\tilde{\lambda}_1(k,T/2)]T/2\}\big|\tilde{\lambda}_1^R(k,T/2)\big\rangle,\end{aligned}$$

where $\zeta = \zeta_1\zeta_2$ and we define $\zeta_2 = \langle\tilde{\lambda}_1^L(k,T/2)|\tilde{\lambda}_1^R(k,0)\rangle$. So $|\tilde{\lambda}_1^R(k,T/2)\rangle$ is the approximate eigenvector of $X_F(k) = \ln\{\exp[X(k,T/2)T/2]\exp[X(k,0)T/2]\}/T$, and the corresponding eigenvalue is $\lambda_1(k) = \ln(\zeta)/T + [\tilde{\lambda}_1(k,T/2) + \tilde{\lambda}_1(k,0)]/2$. Using the definition $\Lambda = \min\{2{\rm Re}[-\lambda_1(k)]\}$, we have $\lim_{T\to\infty}\Lambda = \min\{-{\rm Re}[\tilde{\lambda}_1(k,T/2)+\tilde{\lambda}_1(k,0)]\}$, i.e., Eq. (28).

One of the unique features of non-Hermitian systems is the so-called non-Hermitian skin effect [10,13], where an extensive number of eigenmodes are localized at the boundary of the system and the eigenvalues show extreme sensitivity to the boundary conditions. As for the system studied here, we have verified numerically for a wide range of driving parameters that all the eigenstates of X_F are localized at the boundary when open boundary conditions are used, and the spectrum of X_F is boundary sensitive. So the system described by the time-periodic damping matrix $X(t)$ also exhibits the non-Hermitian skin effect in the sense of time coarsening. But it is different from the undriven system in Ref. [10] with open boundary conditions; the real part of the eigenvalues of X_F is no longer a constant when the driving is slow enough, as shown in Figs. 1(d)–1(f) for the spectrum of X_F with three different driving periods T. Note that although most of the discussion in this section focused on a specific choice of intracell tunneling J_0 and damping rate γ, similar results can be obtained when the parameters are changed.

IV. RELAXATION DYNAMICS

In this section, we study how the periodic driving modifies the relaxation dynamics of the system. The observables of interest are the excitation number profile

$$n_x(t) = \eta_{xA,xA}(t) + \eta_{xB,xB}(t) \quad (30)$$

and the dissipative current to the environment

$$j_x^d(t) = (\gamma_g + \gamma_l)[n_x(t)/2 + i\eta_{xB,xA}(t)] + {\rm c.c.} \quad (31)$$

By the evolution equation (15) of the deviation $\eta(t)$, we can verify that the local excitation number $n_x(t)$ satisfies the continuity equation,

$$\partial_t n_x(t) = j_x^c - j_{x+1}^c - j_x^d(t), \quad (32)$$

where $j_x^c = -iJ_2\eta_{xA,x-1B}(t) + {\rm c.c.}$ represents the coherent current from the unit cell $x-1$ to x. The dissipative current $j_x^d(t)$ leads to the change in the total excitation number $n_{\rm tot}(t) = \sum_x n_x(t)$, i.e.,

$$\partial_t n_{\rm tot}(t) = -\sum_x j_x^d(t). \quad (33)$$

We set the initial state in the Gaussian form [27],

$$\rho(0) = \exp(-\beta\sum_{x\neq x_0,s} c_{xs}^\dagger c_{xs} - \beta'\sum_s c_{x_0s}^\dagger c_{x_0s})/Z, \quad (34)$$

where $Z = {\rm Tr}[\exp(-\beta\sum_{x\neq x_0,s} c_{xs}^\dagger c_{xs} - \beta'\sum_s c_{x_0s}^\dagger c_{x_0s})]$ and $\beta = \ln(\gamma_l/\gamma_g)$. When $\beta' = \beta$, $\rho(0)$ is just the steady state of the system, i.e., $\mathcal{L}(t)[\rho(0)] = 0$. In order to probe the relaxation process of the system, we choose $\beta' \neq \beta$, which describes local excitation at position x_0 upon the steady state. For clarity, we set $\gamma_g = \gamma_l$ and $\beta' \to \infty$ in the following. Then the matrix elements of $\eta(0)$ are $\eta_{x_0A,x_0A}(0) = \eta_{x_0B,x_0B}(0) = -1/2$ and zero otherwise.

The evolution of the total excitation $n_{\rm tot}(t)$ with periodic boundary conditions is shown in Fig. 5. Because of the

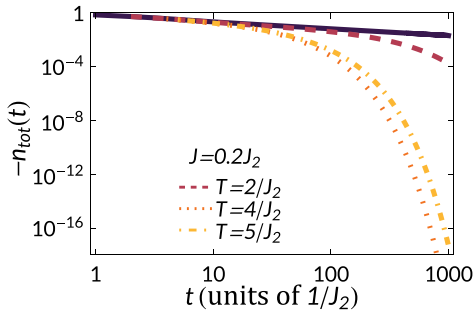

FIG. 5. The evolution of the total excitation number $n_{\rm tot}(t)$ with periodic boundary conditions. The dashed, dotted, and dot-dashed lines are the results for three different driving periods, $T = 2/J_2$, $4/J_2$, and $5/J_2$, respectively. The thick solid line indicates the high-frequency-limit result for comparison. The other parameters are $J_0 = 0.7J_2$, $\gamma_g = \gamma_l = 0.2J_2$, $N = 100$, $x_0 = N/2$, and $J = 0.2J_2$.

nonzero Liouvillian gap induced by the finite-frequency driving, $n_{\rm tot}(t)$ satisfies exponential decay rather than power-law decay. We have verified that the decay rate of $n_{\rm tot}(t)$ is well described by the Liouvillian gap Λ after a transition time, i.e., $n_{\rm tot}(t) \propto \exp(-\Lambda t)$. More precisely, the long-time behavior of $n_{\rm tot}(t)$ is dominated by the modes around the dissipative gap, which provide a decay factor $\sum_{\delta k} \exp\{-[\Lambda + \chi(\delta k)^2]t\} \approx \exp(-\Lambda t) \int d(\delta k) \exp[-\chi(\delta k)^2 t] \sim t^{-1/2} \exp(-\Lambda t) = \exp\{-[\Lambda t + \ln(t)/2]\}$, where χ depends on the parameters of the system. When the evolution time t is very long, the contribution of the logarithmic function in the exponent of $\exp\{-[\Lambda t + \ln(t)/2]\}$ is smaller than the linear function, and the decay factor can be approximated by $\exp(-\Lambda t)$. When the open boundary conditions are used, we find that the initial relaxation process of the localized excitation can still be characterized by the Liouvillian gap Λ of the momentum space Floquet damping matrix $X_F(k)$, but the decay rate of the excitation is close to the bare relaxation rate γ after the initial slow decay stage, as shown in Figs. 6(a) and 6(b). Figure 6(b) shows the evolution of $n_{\rm tot}(t)$ for systems of different sizes where we fix the distance between the initial excitation and the right boundary; the results suggest that the duration of the initial slow relaxation depends on the distance from the localized excitation to the right boundary.

Such a two-stage relaxation process can be attributed to the reflection of the excitation by the boundary, and the reflected wave decays much faster than the incident wave. To illustrate this, we show the evolution of the normalized excitation $n_x(t)/n_{\rm tot}(t)$ in Fig. 7(a). We can see that the peak of $n_x(t)/n_{\rm tot}(t)$ moves to the right at a constant velocity until it reaches the boundary, and the arrival time $t_a \approx 70/J_2$ coincides with the sudden change in damping rate shown in Fig. 6(a). To quantify the propagation velocity of the excitation in the bulk, we define the average position

$$\bar{x}(t) = \sum_x x n_x(t)/n_{\rm tot}(t). \tag{35}$$

Then the propagation velocities v_e [28] are given by

$$v_e = \partial_t \bar{x}(t) \approx \partial_k {\rm Im}[\lambda_1(k)]|_{k=k_c}, \tag{36}$$

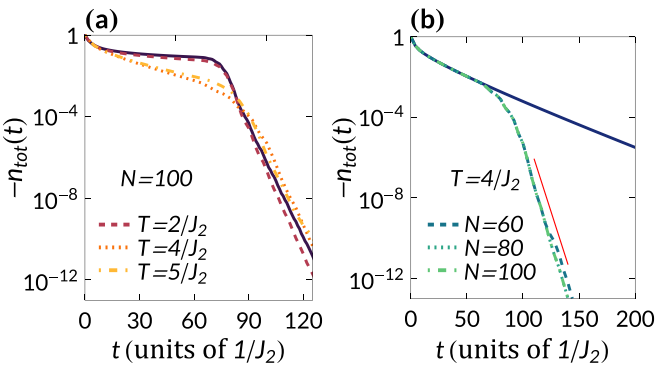

FIG. 6. (a) The evolution of the total excitation number $n_{\rm tot}(t)$ with open boundary conditions. The results for three different driving periods are denoted by different lines, and the thick solid line is the high-frequency-limit result. The initial position of excitation $x_0 = N/2$, and the number of unit cells $N = 100$. (b) Comparison of $n_{\rm tot}(t)$ for systems with different lengths and boundary conditions. The results obtained by applying open boundary conditions are denoted by dashed, dotted, and dot-dashed lines for $N = 60$, 80, and 100, respectively. The thick solid line indicates the periodic boundary result with $N = 100$. The red thin solid line is the exponential fitting $-n_{\rm tot}(t) \propto \exp(-\gamma t)$. The initial position of excitation $x_0 = N - 50$, and the driving period $T = 4/J_2$. The other parameters are $J_0 = 0.7J_2$, $\gamma_g = \gamma_l = 0.2J_2$, $N = 100$, and $J = 0.2J_2$.

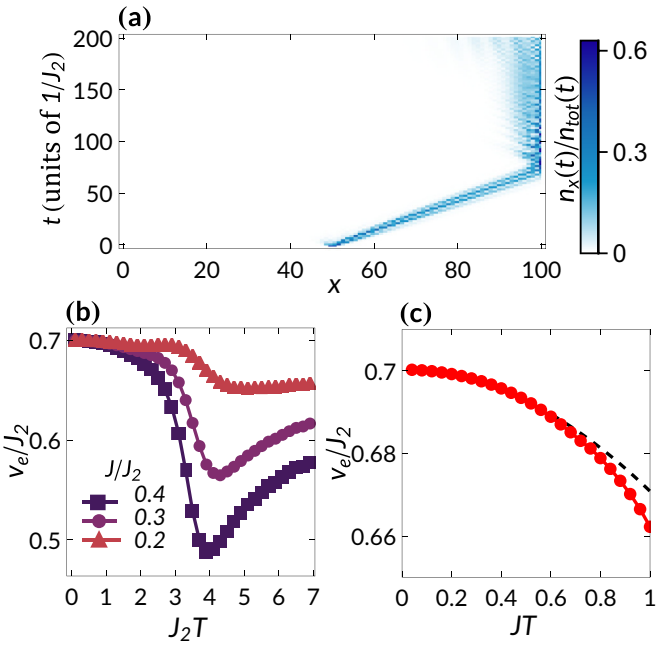

FIG. 7. (a) The evolution of the normalized excitation $n_x(t)/n_{\rm tot}(t)$. The initial position of excitation $x_0 = N/2$, and the number of unit cells $N = 100$. The driving parameters are $J = 0.2J_2$ and $T = 2/J_2$. (b) The propagation velocity of the excitation versus driving period T for three different driving amplitudes, $J = 0.2J_2$, $0.3J_2$, and $0.4J_2$. The results are obtained by the linear fitting of $\bar{x}(t) = x_0 + v_e t$. (c) Comparison of the numerical solution of v_e via linear fitting and the analytical solution $v_e \approx J_0 - \alpha(JT)^2$ for fast driving. The dotted and dashed lines denote the numerical and analytical solutions, respectively. The other parameters are $J_0 = 0.7J_2$ and $\gamma_g = \gamma_l = 0.2J_2$.

where $\lambda_1(k)$ is the eigenvalue of $X_F(k)$ with the largest real part for given k and k_c corresponds to the largest $\mathrm{Re}[\lambda_1(k)]$. In Fig. 7(b), we show the typical situations of the velocity v_e as a function of driving parameters. The results suggest that a moderate increase in the driving period can lead to a substantial decrease of the propagation velocity of the excitation. In the case of fast driving, we can also obtain the velocity v_e via the approximate Floquet damping matrix $X_F^{(2)}(k)$ and the relation $v_e \approx \partial_k \mathrm{Im}[\lambda_1(k)]|_{k=k_c}$; the result is

$$v_e \approx J_0 - \alpha(JT)^2, \tag{37}$$

where the coefficient $\alpha = \{J_0(4J_2^2 - 4J_0^2 - \gamma^2) - 4J_2^2\sqrt{J_2^2 - J_0^2}\sin[2\arccos(J_0/J_2)]\}/[24(4J_0^2 - 4J_2^2 - \gamma^2)]$. A comparison of the analytic expression $v_e \approx J_0 - \alpha(JT)^2$ and the numerical results of v_e using the linear fitting of $\bar{x}(t)$ is shown in Fig. 7(c); the two are in good agreement.

When the excitation reaches the boundary of the system, it is effectively trapped there. It is known that the decay rates of the eigenmodes under open boundary condition are no longer a constant γ for slower drives, but their deviations from γ are approximately an order of magnitude smaller than γ, as shown in Figs. 1(d)–1(f). This is why the overall decay rate of the excitation is close to γ when it reaches the boundary. The decay rate of the excitation will gradually approach the open boundary Liouvillian gap over a long time evolution that is slightly smaller than γ for slower drives. If the bulk loss of the excitation is small enough in this case, a significant portion of the excitation will escape from the boundary. This is the so-called non-Hermitian edge burst [11]. For the model studied here, the site-resolved loss of excitation is given by

$$P_x = -\int_0^\infty j_x^d(\tau)d\tau. \tag{38}$$

We adopt the relative edge loss L_{rel} introduced in Ref. [11] to quantify the edge burst,

$$L_{\mathrm{rel}} = P_{\mathrm{edge}}/P_{\mathrm{min}}, \tag{39}$$

where $P_{\mathrm{edge}} = P_N$ and $P_{\mathrm{min}} = \min[P_{x_0}, P_{x_0+1}, \ldots, P_{\mathrm{edge}}]$ is the minimum of P_x between the initial position x_0 and the right edge. The existence and absence of the edge burst are characterized by $L_{\mathrm{rel}} \gg 1$ and $L_{\mathrm{rel}} \sim 1$, respectively [11]. Figure 8(a) shows the site-resolved loss P_x in the fast-driving limit $T \to 0$; we notice that P_x decreases rapidly in the bulk, but an exceptionally high peak appears at the right edge of system. When the driving period increases (but is smaller than the critical driving period $T \approx 4/J_2$), the bulk loss characterized by the Liouvillian gap increases, and the edge-loss peak will be reduced. We illustrate this in Fig. 8(b) by the relative edge loss L_{rel} as a function of driving period T. These findings are in agreement with the results in Ref. [11], which studied the escape probability in lattices described by a static non-Hermitian Hamiltonian.

V. CONCLUSION

In summary, we studied the relaxation dynamics of the SSH model with single-particle loss and time-periodic modulation imposed on intracell tunnelings. For periodic boundary conditions, we found that the system has a zero Liouvillian gap in the infinite-frequency driving limit, while the finite-frequency driving opens the Liouvillian gap and changes the system relaxation from algebraic to exponential. Along with the increasing of the driving period, the Liouvillian gap increases until a critical driving period is reached, and for a sufficiently slow drive, the Liouvillian gap converges to a smaller nonzero value. By investigating the time evolution of localized excitation, we observed that the damping of the excitation in open boundary systems can still be interpreted by the Liouvillian gap derived from the momentum space damping matrix. This result holds true until it reaches the boundary. After reaching the boundary, the eigenvalue spectrum of the open boundary chain starts to govern the relaxation dynamics, and the decay rate of the excitation approaches the open boundary Liouvillian gap asymptotically. The duration of the transition relaxation depends on the propagation velocity of the excitation, and the spread of the excitation can be slowed down by increasing the driving period and amplitude.

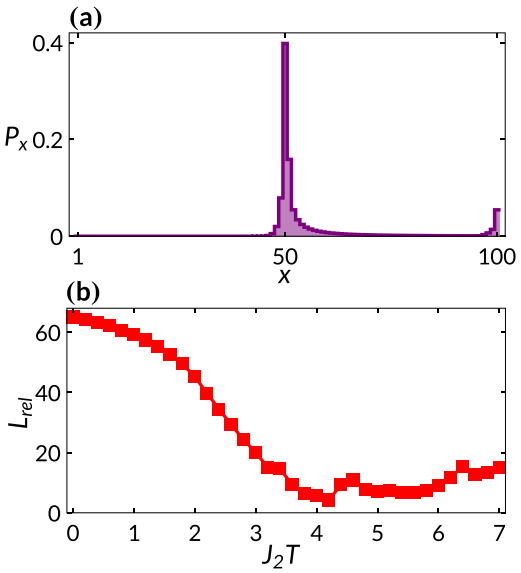

FIG. 8. (a) The site-resolved loss of excitation P_x in the fast-driving limit $T \to 0$. (b) The relative edge loss $L_{\mathrm{rel}} = P_{\mathrm{edge}}/P_{\mathrm{min}}$ versus driving period T for driving amplitude $J = 0.2J_2$. The other parameters are $J_0 = 0.7J_2$, $\gamma_g = \gamma_l = 0.2J_2$, and $N = 100$.

ACKNOWLEDGMENTS

This work is supported by National Natural Science Foundation of China (Grants No. 12105245, No. 12074340 and No. 12175033) and the Fundamental Research Funds of Zhejiang Sci-Tech University (Grant No. 21062106-Y), as well as National Key R&D Program of China (No. 2021YFE0193500).

APPENDIX: DERIVATION OF THE SINGLE-PARTICLE CORRELATION-MATRIX EVOLUTION EQUATION

According to the master equation (4) and the definition of the single-particle correlation matrix (10) in the main text, the time evolution of $\phi_{mn}(t)$ satisfies the following equation:

$$\partial_t \phi_{mn}(t) = \mathrm{Tr}[c_m^\dagger c_n\{-i[H(t), \rho(t)] + \mathcal{D}[\rho(t)]\}]. \tag{A1}$$

To proceed, we can use the cyclic property of the trace to rewrite Eq. (A1) as

$$\partial_t \phi_{mn}(t) = -i\mathrm{Tr}\{[c_m^\dagger c_n, H(t)]\rho(t)\} + \sum_{x\kappa} \mathrm{Tr}\{(L_{x\kappa}^\dagger [c_m^\dagger c_n, L_{x\kappa}] + [L_{x\kappa}^\dagger, c_m^\dagger c_n] L_{x\kappa})\rho(t)\}. \tag{A2}$$

For the quadratic Hamiltonian $H(t) = \sum_{\alpha\beta} h_{\alpha\beta}(t) c_\alpha^\dagger c_\beta$ and the jump operators of linear form $L_{xl} = \sum_\alpha D_{xl,\alpha} c_\alpha$ and $L_{xg} = \sum_\alpha D_{xg,\alpha} c_\alpha^\dagger$ that we used, the commutation relations on the right-hand side of Eq. (A2) can be simplified as

$$[c_m^\dagger c_n, H(t)] = \sum_{\alpha\beta} h_{\alpha\beta}(t)(\delta_{n\alpha} c_m^\dagger c_\beta - \delta_{m\beta} c_\alpha^\dagger c_n), \tag{A3}$$

$$L_{xl}^\dagger [c_m^\dagger c_n, L_{xl}] + [L_{xl}^\dagger, c_m^\dagger c_n] L_{xl} = -\sum_{\alpha\beta} (\delta_{m\alpha} D_{xl,\beta}^* D_{xl,\alpha} c_\beta^\dagger c_n + \delta_{n\beta} D_{xl,\beta}^* D_{xl,\alpha} c_m^\dagger c_\alpha), \tag{A4}$$

$$L_{xg}^\dagger [c_m^\dagger c_n, L_{xg}] + [L_{xg}^\dagger, c_m^\dagger c_n] L_{xg} = \sum_{\alpha\beta} (\delta_{n\alpha} D_{xg,\beta}^* D_{xg,\alpha} c_\beta c_m^\dagger + \delta_{m\beta} D_{xg,\beta}^* D_{xg,\alpha} c_n c_\alpha^\dagger). \tag{A5}$$

Inserting Eq. (A3)–(A5) into Eq. (A2), we obtain

$$\begin{aligned}\partial_t \phi_{mn} = {} & i \sum_\alpha \phi_{\alpha n} h_{\alpha m}(t) - \phi_{m\beta} h_{n\beta}(t) \\ & - \sum_{x\alpha} [D_{xl,\alpha}^* D_{xl,m} \phi_{\alpha n} + D_{xl,n}^* D_{xl,\alpha} \phi_{m\alpha} \\ & + D_{xg,\alpha}^* D_{xg,n} \phi_{m\alpha} + D_{xg,m}^* D_{xg,\alpha} \phi_{\alpha n}] \\ & + 2 \sum_x D_{xg,m}^* D_{xg,n},\end{aligned} \tag{A6}$$

where we omit the time dependence of $\phi(t)$ for simplicity. By defining two matrices, $(M_l)_{mn} = \sum_x D_{xl,m}^* D_{xl,n}$ and $(M_g)_{mn} = \sum_x D_{xg,m}^* D_{xg,n}$, we can rephrase Eq. (A6) in matrix form,

$$\partial_t \phi(t) = i[h^T(t), \phi(t)] - \left\{M_l^T + M_g, \phi(t)\right\} + 2M_g. \tag{A7}$$

For the model we studied, the nonzero elements of $h(t)$ and D are $h_{xA,xB}(t) = h_{xB,xA}^*(t) = J_1(t)$, $h_{xB,x+1A} = h_{x+1A,xB}^* = J_2$, $D_{xl,xA} = iD_{xl,xB} = \sqrt{\gamma_l/2}$, and $D_{xg,xA} = -iD_{xg,xB} = \sqrt{\gamma_g/2}$.

[1] M. Aidelsburger, M. Lohse, C. Schweizer, M. Atala, J. T. Barreiro, S. Nascimbène, N. R. Cooper, I. Bloch, and N. Goldman, Measuring the Chern number of Hofstadter bands with ultracold bosonic atoms, Nat. Phys. **11**, 162 (2015).

[2] T. Čadež, R. Mondaini, and P. D. Sacramento, Dynamical localization and the effects of aperiodicity in Floquet systems, Phys. Rev. B **96**, 144301 (2017).

[3] N. Y. Yao, A. C. Potter, I.-D. Potirniche, and A. Vishwanath, Discrete Time Crystals: Rigidity, Criticality, and Realizations, Phys. Rev. Lett. **118**, 030401 (2017).

[4] L. Zhou, Floquet engineering of topological localization transitions and mobility edges in one-dimensional non-Hermitian quasicrystals, Phys. Rev. Res. **3**, 033184 (2021).

[5] H. Keßler, P. Kongkhambut, C. Georges, L. Mathey, J. G. Cosme, and A. Hemmerich, Observation of a Dissipative Time Crystal, Phys. Rev. Lett. **127**, 043602 (2021).

[6] D. Dwiputra, J. S. Kosasih, A. Sulaiman, and F. P. Zen, Driving-assisted open quantum transport in qubit networks, Phys. Rev. A **101**, 012113 (2020).

[7] H. Weimer, M. Müller, I. Lesanovsky, P. Zoller, and H. P. Büchler, A Rydberg quantum simulator, Nat. Phys. **6**, 382 (2010).

[8] B. P. Lanyon, C. Hempel, D. Nigg, M. Müller, R. Gerritsma, F. Zähringer, P. Schindler, J. T. Barreiro, M. Rambach, G. Kirchmair, M. Hennrich, P. Zoller, R. Blatt, and C. F. Roos, Universal digital quantum simulation with trapped ions, Science **334**, 57 (2011).

[9] T. Haga, M. Nakagawa, R. Hamazaki, and M. Ueda, Liouvillian Skin Effect: Slowing Down of Relaxation Processes without Gap Closing, Phys. Rev. Lett. **127**, 070402 (2021).

[10] F. Song, S. Yao, and Z. Wang, Non-Hermitian Skin Effect and Chiral Damping in Open Quantum Systems, Phys. Rev. Lett. **123**, 170401 (2019).

[11] W. T. Xue, Y. M. Hu, F. Song, and Z. Wang, Non-Hermitian Edge Burst, Phys. Rev. Lett. **128**, 120401 (2022).

[12] P. He, Y. G. Liu, J. T. Wang, and S. L. Zhu, Damping transition in an open generalized Aubry-Andr-Harper model, Phys. Rev. A **105**, 023311 (2022).

[13] K. Kawabata, M. Sato, and K. Shiozaki, Higher-order non-Hermitian skin effect, Phys. Rev. B **102**, 205118 (2020).

[14] W. P. Su, J. R. Schrieffer, and A. J. Heeger, Solitons in Polyacetylene, Phys. Rev. Lett. **42**, 1698 (1979).

[15] E. J. Meier, F. A. An, and B. Gadway, Observation of the topological soliton state in the Su–Schrieffer–Heeger model, Nat. Commun. **7**, 13986 (2016).

[16] G. Lindblad, On the generators of quantum dynamical semigroups, Commun. Math. Phys. **48**, 119 (1976).

[17] D. Malz and A. Nunnenkamp, Current rectification in a double quantum dot through fermionic reservoir engineering, Phys. Rev. B **97**, 165308 (2018).

[18] C. M. Dai, Z. C. Shi, and X. X. Yi, Floquet theorem with open systems and its applications, Phys. Rev. A **93**, 032121 (2016).

[19] C. M. Dai, Z. C. Gu, and X. X. Yi, Discrete time-crystalline order in Bose–Hubbard model with dissipation, New J. Phys. **22**, 023026 (2020).

[20] G. Floquet, Sur les équations diffrentielles linéaires à coefficients périodiques, Ann. Sci. Ec. Norm. Super. **12**, 47 (1883).

[21] T. N. Ikeda and M. Sato, General description for nonequilibrium steady states in periodically driven dissipative quantum systems, Sci. Adv. **6**, eabb4019 (2020).

[22] J. Wong, Results on certain non-Hermitian Hamiltonians, J. Math. Phys. **8**, 2039 (1967).

[23] E. Persson, T. Gorin, and I. Rotter, Decay rates of resonance states at high level density, Phys. Rev. E **54**, 3339 (1996).

[24] M. van Caspel and V. Gritsev, Symmetry-protected coherent relaxation of open quantum systems,, Phys. Rev. A **97**, 052106 (2018).

[25] F. Casas and A. Murua, An efficient algorithm for computing the Baker–Campbell–Hausdorff series and some of its applications, J. Math. Phys. **50**, 033513 (2009).

[26] E. Frank, On the zeros of polynomials with complex coefficients, Bull. Amer. Math. Soc. **52**, 144 (1946).

[27] H. M. Wiseman and G. J. Milburn, *Quantum Measurement and Control* (Cambridge University Press, Cambridge, 2009).

[28] Z. Gong, Y. Ashida, K. Kawabata, K. Takasan, S. Higashikawa, and M. Ueda, Topological Phases of Non-Hermitian Systems, Phys. Rev. X **8**, 031079 (2018).